Solid Earth Discuss., 4, 131–172, 2012
www.solid-earth-discuss.net/4/131/2012/
doi:10.5194/sed-4-131-2012

Solid Earth Discussions

Geomagnetic jerks characterization via spectral analysis

B. Duka[1], A. De Santis[2,3], M. Mandea[4,5], A. Isac[6], and E. Qamili[2]

[1]Faculty of Natural Sciences, University of Tirana, Tirana, Albania
[2]Istituto Nazionale di Geofisica e Vulcanologia, Roma, Italy
[3]Universita' G. D'Annunzio, Chieti, Italy
[4]Directorate for Strategy and Programmes, Centre National d'Etudes Spatiale, Paris, France
[5]European Center for the Arctic, Université de Versailles, Guyancourt, France
[6]Geological Institute of Romania, Bucharest, Romania

Received: 12 December 2011 – Accepted: 13 December 2011 – Published: 20 January 2012

Correspondence to: B. Duka (bejo.duka@unitir.edu.al)

Published by Copernicus Publications on behalf of the European Geosciences Union.

Abstract

In this study we have applied spectral techniques to analyze geomagnetic field time-series provided by observatories, and compared the results with those obtained from analogous analyses of synthetic data estimated from models. Then, an algorithm is here proposed to detect the geomagnetic jerks in time-series, mainly occurring in the Eastern component of the geomagnetic field. Applying such analysis to time-series generated from global models has allowed us to depict the most important space-time features of the geomagnetic jerks all over the globe, since the beginning of XXth century. Finally, the spherical harmonic power spectra of the third derivative of the main geomagnetic field has been computed from 1960 to 2002.5, bringing new insights to understanding the spatial evolution of these rapid changes of the geomagnetic field.

1 Introduction

Studies of discrete time-series of different physical quantities are widely interesting not only for their forecasting, but also for defining the nature and behavior of the underlying physical phenomena. Different methods of time-series analyses have been used to study the geomagnetic field which is, at all times, subject to temporal variations on a wide range of time scales. Most of the rapid variations are linked to the solar activity and solar variability (many different forms include solar flares, coronal mass ejections, solar wind sector boundaries, coronal hole streams), as well as in the Earth's environment (interactions between the solar wind and the core field). Most of the slow variations are generated in the outer fluid core (changes in the fluid flow). The temporal variations in the geomagnetic field cover a huge range of time-scales, from seconds to hours (external in origin), from months to decades (overlapping between external and internal changes), or from millennial to reversals (internal variations). Here, we focus on the analysis of changes in geomagnetic field, as mainly recorded by magnetic data provided by magnetic observatories. This work is dedicated to analyze the short-term (likely internal) variations, observed in the geomagnetic field.

SED
4, 131–172, 2012

The short-term variations of geomagnetic field, internal in origin, the so-called geomagnetic jerks (Courtillot et al., 1978), can be defined as sudden changes (a V-shape like change) in the slope of the secular variation (SV), i.e. the first time derivative of the Earth's magnetic field, or an abrupt (step-like) change in the secular acceleration (SA), i.e. the second time derivative. As a very first approximation, the secular variation can be described as a set of linear changes over some years to some decades, separated by geomagnetic jerks occurring on a time-scale of a few months when the nearly constant secular acceleration changes sign (and, eventually, its magnitude) abruptly. For a more detailed characterization of geomagnetic jerks, we have to consider the findings of Alexandrescu et al. (1996). Indeed, when the wavelet technique has been applied to series of monthly means, it appears that the event reveals a singular behavior with a regularity close to 1.5. This interesting behavior is useful to analyze the geomagnetic jerks at the place of their origin, indeed the top of the core. However, in the present analysis, we do not consider geomagnetic jerks as singularities defined as discontinuities of some α^{th} derivative of the signal, but as an integer derivative (i.e. second one).

Nowadays, it is almost accepted that geomagnetic jerks are internal in origin i.e. they are produced by fluid flows at the top of the outer core. Some attempts to explain their physical origin have been done. One of them, found in Bloxham et al. (2002), explains their origin by a combination of a steady flow and a simple time-varying, axisymmetric, equatorially symmetric, toroidal zonal flow, consistent with torsional oscillations in the Earth's core.

Usually, geomagnetic jerks are particularly visible in the Eastward component (Y), which is supposed to be the least affected by the external fields (Mandea et al., 2010). More affected by external field are the Northward component (X) and, slightly less, the vertical downward component (Z). An easy method to determine the epoch when a geomagnetic jerk occurs is to approximate secular variation time-series by straight lines and to consider the intersection point of such lines as the date of an event (Chau et al., 1981; Stewart and Whaler, 1992). During the last two decades, more powerful

SED
4, 131–172, 2012

methods to detect geomagnetic jerks and to estimate their location and duration have been developed. For example, the wavelet analysis have been largely applied to the monthly mean series provided by different geomagnetic observatories (Alexandrescu et al., 1995; Alexandrescu et al., 1996; Chambodut et al., 2005), or a statistical time-series model has been used to analyze monthly means of the geomagnetic Eastward component at different observatories (Nagao et al., 2003).

We have used three different methods of analyses to study time-series of geomagnetic field components and secular variations, with particular attention to the Y component. All methods are essentially spectral analyses. Two of them, the Short Time Fourier Transform (STFT) and Discrete Wavelet Transform (DWT), derive directly as natural developments of Fourier Analyses, while the third one is a spatial spectral analysis in spherical harmonics performed at different successive epochs. The first two methods are essentially single-station time-series analyses, while the third one is a global spherical harmonic analysis. In this paper, we present the results of applying these methods on time-series of geomagnetic field of different observatories or time-series of synthetic data generated by different models. Thereafter, we discuss the results and conclude.

2 Data: observed and model-based temporal series

Before presenting the applied methods, we describe the used data. The first kind of dataset, which are real data, are composed of time-series of geomagnetic field components recorded by geomagnetic observatories. They are chosen to be longer than 50 years and located as far as possible from each other. In addition, some synthetic data have been generated by means of specific function (see Sect. 3.1.2) or by specific composition (see Sect. 3.2.2) that simulate geomagnetic jerks, in order to optimize the real data processing. We then generate time-series of geomagnetic field components, secular variation or secular acceleration from two geomagnetic field models described below, for a regular (uniform) grid of points over the Earth, allowing to investigate specific,

SED
4, 131–172, 2012

large scale behavior of jerks over the globe. We also use one of these models to investigate the third derivative of the Gauss coefficients.

2.1 Observatory data

In this work, we have considered several observatories: Alibag (ABG), Apia (API), Chambon La Foret (CLF), Eskdalemuir (ESK), Gnangara (GNA), Hermanus (HER), Huancayo (HUA), Kakioka (KAK), Lerwick (LER), Pilar (PIL), Sitka (SIT), Vassouras (VSS), for which hourly means have been downloaded[1]. From the original hourly means of these observatories, their monthly mean values series have also been calculated.

A long and typical time-series the geomagnetic field has been recorded at Niemegk Observatory (before 1932 observations were made nearby at Potsdam, then Seddin). The annual means series of X, Y, Z components and the differences of sequential values ($\Delta X/\Delta t$, $\Delta Y/\Delta t$, $\Delta Z/\Delta t$, with $\Delta t = 1$ year) are presented in Fig. 1. The monthly means series of X, Y, Z components show the same behavior as the annual means, but the differences of sequential values ($\Delta X/\Delta t$, $\Delta Y/\Delta t$, $\Delta Z/\Delta t$, with $\Delta t = 1$ month) , show that they are bearing a great amount of noise not filtered from the signal (Fig. 1). Therefore, to remove most of the uncorrelated noise, we apply a moving average approach (Olsen and Mandea, 2007) to calculate a smoothed secular variation (see discussion in 3.2.3). A glance at these plots stimulates a few remarks. First, the same field component has the same behavior in both time-series, however, mainly for the X component the noise level is higher in the monthly means. Second, the secular variation (first differences of the component values) presents changes in its trend in the annual curves and less clear in the monthly ones.

[1] http://spidr.ngdc.noaa.gov/spidr/

SED
4, 131–172, 2012

Amongst the considered observatories, 4 of them, indicated in Table 1, have been chosen as representative for our analyses. These observatories have been selected because their recordings are uninterrupted over more than 50 years, and they are located at different latitudes and longitudes.

2.2 Geomagnetic models

Time-series of the geomagnetic field components, their secular variation and acceleration are generated from two models, CM4 (Sabaka et al., 2004) and Gufm1 (Jackson et al., 2000).

The CM4 model (Sabaka et al., 2004) entails the parameterisation and coestimation of fields associated with the major magnetic field sources in the near-Earth regime from field measurements taken from ground-based observatories and satellite missions (POGO, Magsat, Ørsted, CHAMP). It supplies the local X, Y, Z components of the **B** field vector from the main, lithosphere, primary and induced magnetosphere, primary and induced ionosphere, and toroidal field sources. Two evaluations of the main field are accommodated per two given spherical harmonic degree ranges for the span period 1960–2002.5 http://core2.gsfc.nasa.gov/CM/CM4_A.html. The capacity of this model to represent geomagnetic jerks has been already investigated (Sabaka et al., 2002; Chambodut and Mandea, 2005). Here, we use the time-series of third derivative of Gauss coefficients (1960–2002.5) to study any possible relation between maxima of the corresponding spherical harmonic power spectra and geomagnetic jerk occurrence.

The Gufm1 model (Jackson et al., 2000), is based on a massive compilation of historical observations of the geomagnetic field (from 1590 to 1990). For the period before 1800, more than 83 000 individual observations of magnetic declination were recorded at more than 64 000 locations; more than 8000 new observations come from the 17th century alone. Since no intensity data are available prior to 1840, the axial dipole component is linearly extrapolated back before this date. The time-dependent field model constructed from this dataset is parameterised spatially in terms

SED
4, 131–172, 2012

of spherical harmonics and temporally in B-splines, using a total of 36 512 parameters http://jupiter.ethz.ch/~cfinlay/gufm1.html. This model has been used to generate monthly series of X, Y, Z components and their secular variations on a regular grid on the Earth's surface.

3 Methods: characteristics and application to datasets

3.1 Short Time Fourier Transform (STFT)

3.1.1 STFT – definition and representation

It is well known, that the Fourier analysis breaks down a signal into constituent harmonics of different frequencies. For regularly sampled data, Fourier analysis is performed using the discrete Fourier transform (DFT). The fast Fourier transform (FFT) is an efficient algorithm for computing the DFT of an input sequence x of length N (see Appendix A).

Using the Fourier transform of a signal, it is impossible to indicate when particular events (such as drifts, trends, abrupt changes, etc.) appear within the time-series. This deficiency can be corrected by applying the Fourier transform only to small sections of the signal at successive times, a technique called windowing the signal (Gabor, 1946) or the Short-Time Fourier Transform (STFT) (see Appendix A). The STFT maps a signal into a two-dimensional function of time and frequency and can provide information about both time and frequency, thus characterizing a particular event present in the analyzed time-series.

In order to detect particular events in long time-series of the geomagnetic field components, secular variation or secular acceleration, we have used the "specgram" function of Matlab7 software (Matlab release notes, 2004), which computes the windowed discrete-time Fourier transform of a signal using a sliding window (see Appendix A). The spectrogram is the magnitude of this function expressed in decibel (dB). Different

SED
4, 131–172, 2012

kinds of windows have been tested, with a different length and different overlaps, providing a sampling frequency: $f_s = 1$ (month^{-1} or year^{-1} according to the kind of analysis). To avoid a plain spectrum in the case of geomagnetic field components, an average value of series is subtracted from each input data.

The most used windows have a Gaussian-like form (e.g. Blackman, Bohman, Chebyshev, Gaussian, Hamming, Hann, Parzen windows, to say some), and we notice that, on one hand, the results of spectrogram analyses almost do not depend on the form of window. On the other hand, the results considerably depend on the length of the signal. The length of window and overlaps should be adapted to signal length.

3.1.2 SFTF – applied to a synthetic signal

Mathematically, the jerk events are discontinuities (breakdowns) of the second derivatives of the geomagnetic field components. To test the real effectiveness of different techniques, we consider a synthetic signal which has such breakdowns in its second derivative. Then, we will take the advantage of the results found to apply the same processing scheme to real data.

We consider the following synthetic signal as defined in the interval $-0.5 \le t \le 0.5$:

$$f(t) = \begin{cases} \exp(-40 \cdot t^2) \text{ for } -0.5 \le t < 0 \\ \exp(-10 \cdot t^2) \text{ for } 0 \le t \le 0.5 \end{cases}, \quad (1)$$

and sampled at every $\Delta t = 10^{-3}$. We have actually rescaled the temporal abscissa as time = 500 + $t \cdot 1000$, i.e. in the interval of time 0–1000 (see Fig. 2). We chose such signal, because it and its first derivative have a smooth behavior during the whole interval, but the signal has the second derivative breakdown exactly at time = 500 (t = 0) and near this point it shows a jerk-like behavior. One can not detect any breakdown in the signal plot (Fig. 2, upper left) and in the spectrogram of the signal (Fig. 2 down left). The spectrogram of the first differences shows a clear breakdown close to the real one at time = 500 (Fig. 2, down right). Notice that the abscissa length is slightly

SED
4, 131–172, 2012

different for signals and spectrograms, as for the chosen parameters (*nfft* = 1000, $f_s = 1$, Hamming window length = 12, overlaps = 10) the time length of the signal changes in its spectrogram (1000 becomes 990).

3.1.3 SFTF – applied to annual mean series

We present here some results of SFTF analyses, firstly applied to NGK series of 116 averaged annual means (from 1890 to 2005). In case of X, Y, Z component series, from the original data an average value of series is subtracted. In the spectrograms of these field series and their first differences (see Fig. 3) the same kind of window (Hamming) and same lengths of window (12 values) and overlaps (10 values) are used. The spectrograms of different components show particular events at different epochs, most of them not corresponding to the known geomagnetic jerks found in literature (e.g. Mandea et al., 2010). The spectrograms of the first differences of the consecutive annual values, show the evidence of particular events likely to be the geomagnetic jerks especially in the case of the Y component. In this case, there is a clear evidence of a special event around 1969, that corresponds to the first noted geomagnetic jerk. One can also note some evidence of the geomagnetic jerks of 1901 and 1991, but little evidence of other known events. There is very little evidence of the 1999 event, but being close to the 1991 event and having less abrupt changes of the slopes, it seems like to have only one large event. Instead, the known event of 1925 can be detected from the maximum of spectrogram. This will be explained by greatest change of the slope characterizing this event.

3.1.4 SFTF – applied to monthly mean series

In case of monthly means of the geomagnetic field components, the first differences represent very irregular and noisy signals (Fig. 1). In order to minimize this noise, mainly produced by the external field variations (ionospheric and magnetospheric variations), a moving average is applied to monthly means of secular variation. For

SED
4, 131–172, 2012

example, for the Y component, less influenced by external fields, the secular variation (SV_y) is calculated as:

$$SV_y(i) = \frac{\sum_{k=0}^{n-1} Y(i+k) - \sum_{l=1}^{n} Y(i-l)}{n} \quad (2)$$

where $n = 1,2,3,4\ldots12$, for different representatives of SV_y with different size of the running window. The larger running window is, the smoother and more de-noised the signal is. Usually, studies on geomagnetic jerks considered n =12-month moving average (e.g. Mandea et al., 2000).

Applying the "specgram" function to the monthly series of Y secular variation (from (2)) with n = 12-month moving average, and the same kind of window, the same length and overlaps as in the case of annual series, we obtain the spectrogram shown in Fig. 4. We can detect the geomagnetic jerks around the years 1900, 1969 and 1990, which are better underlined here than in the case of annual average differences. The reason is that the technique provides better results when the data sets are longer or denser. It is clear that this method is not suitable to be applied to annual or monthly means, directly. For this reason, we need to find different ways to extract the maximum of information from temporal series. In order to improve the results of the spectrogram method, we consider important to de-noise the geomagnetic signals, one efficient technique for de-noising being the use the wavelets analyses.

3.2 Discrete Wavelet Transform (DWT)

3.2.1 DWT – definition and representation

For the self-consistency of this paper, some generalities about the DWT are summarized in the following. Wavelet analysis represents a windowing technique with variable-sized regions, normally with long time intervals providing more precise low-frequency

SED
4, 131–172, 2012

information, and shorter time intervals with high-frequency information. Wavelet analysis is capable of revealing aspects of data like trends, breakdown points, discontinuities in higher derivatives, and self-similarity. It is also used to compress or de-noise a signal without appreciable degradation (e.g. Kumar and Georgiu, 1994).

Similar to Fourier analysis, wavelet analysis is the breaking up of a signal into shifted and scaled versions of the original (or *mother*) wavelet (see Appendix B).

According to DWT analysis (see Appendix B), any signal $s(t)$ can be presented as the sum of approximations and fine details (see Eq. B8):

$$s = a_J + \sum_{j \le J} d_j$$

In order to better identify discontinuities in the second derivative of the geomagnetic field components (monthly mean values series) registered at different observatories, we consider different kinds of wavelet shapes and level parameters among those proposed by Matlab software http://www.mathworks.com/help/toolbox/wavelet/. Our final choice is based on the aim to detect a "rupture" in the j-th derivative, selecting a sufficiently regular wavelet with at least j vanishing moments.

The presence of noise makes identification of discontinuities more complicated. If the first levels of the decomposition can be used to eliminate a large part of noise, the "rupture" is sometimes visible only at deeper levels in the decomposition.

After many attempts, we have found that the kind of wavelets detecting successfully the second order derivative change in the known signal (1) is the Daubechies wavelet (Daubechies, 1992), of order 4 (Db4) at level 2 of the signal decomposition:

$$s = a_2 + d_2 + d_1, \tag{3}$$

where the decomposition (see Eq. B8) ends at $J = 2$. The results show anomalous values of coefficients d_1 and d_2 exactly where (time = 500) the signal (1) has the second derivative breakdown. This breakdown is better localized by the anomalous values of d_1 coefficients.

SED
4, 131–172, 2012

3.2.2 Geomagnetic data de-noising by using DWT

Synthetic signal

In order to define empirically the best way for applying DWT technique to the signal de-noising, we generate a series of several exponential spikes like (1) with different slopes (Fig. 5). In order to get a signal more like the secular variation provided by a geomagnetic observatory, we add to the original synthetic signal a colored noise (see Appendix C). These changes provide a more realistic noise (more like a secular variation signal) with the amplitude of the noise of about 15 % of the signal itself. The composed signal and its spectrogram are shown in Fig. 5.

After applying DWT with different wavelets, the most appropriate ones in order to get the best de-noised signal are the Daubechies wavelets of order 3 and level 4. Such de-noised signal and its spectrogram are also shown in Fig. 5. According to these spectrograms, we can note:

- The breakdowns of the second derivative shown in the spectrogram of the de-noised signal (first difference series) coincide with clear separations of the spectrogram lobes; the maxima of these lobes correspond to the extremes (maxima or minimums) of the de-noised signal.
- The more abrupt the changes of the slopes of the signal, the more closer each-other of the respective spectrogram lobes are; in an extreme case, it is not possible to distinguish the separation between spectrogram lobes representing two very close different slopes.
- Defining an appropriate de-noising process and applying it to the composed signal (original one and noise), a spectrogram similar to that of the original signal is obtained, which can be used to easily identify the abrupt changes of slopes.

These ascertainments indicate that in order to detect jerk-like events by the STFT method, we should study the spectrogram of the de-noised secular variation.

SED
4, 131–172, 2012

Real data

We have applied this technique of de-noising the signal before getting the spectrogram of SV_Y monthly series of 4 observatories previously described. The obtained results are shown in Fig. 6, where the breakdowns of the spectrogram lobes correspond to the time occurrences of the jerk-like events. When there are abrupt changes in the slope of the real secular variation signal (see for example KAK observatory around 1952), the same behavior as in the composed signal can be noted with a breakdown of the spectrogram corresponding to the middle of the slope.

Fig. 6 shows that generally the spectrograms of the de-noised secular variation of different observatories reflect a different behavior of the secular variation in these observatories. In the low latitude observatories (API) more changes in the slope of the secular variation can be better detected than at higher latitude observatories. These changes are smaller in amplitude and longer in time and reflect long-term events, such as 1950–1954 and 1996–1998 at API observatory. From the spectrogram corresponding to API observatory, it is possible to confirm some geomagnetic jerks around 1954 and 1978. At higher latitude observatories (NGK) the de-noising process smoothed the secular variation in such a way that the geomagnetic jerks noted in the original signals (as around 1925 and 1978) are difficult to detect in the respective spectrograms. However, in NGK spectrogram, geomagnetic jerks around 1901, 1969, 1990 and 1999 can be detected. Spectrograms for the middle latitude observatories (HER and KAK) indicate some different times for geomagnetic jerks. For HER observatory it is possible to note a less marked event around 1954, a stronger one around 1986 and the strongest event around 1995. The change in the slope centered in 1972 lasts here from 1968 to 1978 and can not be considered as a geomagnetic jerk signature. For the KAK observatory, we can identify a geomagnetic jerk around 2000, and hardly identify events nearly by 1957 and 1969. Although there are clear changes in the secular variation of KAK observatory before 1959, they might be also due to the quality of data.

SED
4, 131–172, 2012

3.2.3 DWT applied to the monthly mean series

To determine the second derivative breakdown of the geomagnetic field components, we apply DWT to long time-series of geomagnetic field recorded at different geomagnetic observatories. The results underline different kind of events, including some of the well-known geomagnetic jerks. Better results, when jerks are easily detected, have been obtained when the DWT analyses is applied to the Y component secular variation, calculated by the moving average window of 12 months. Before applying the DWT analyses, we have applied a de-noising procedure on the secular variation signal.

Synthetic signal

The composed signal (several exponential spikes and a colored noise) is de-noised by using Daubechies wavelets of order 3 and level 4, and represented in Fig. 5. The obtained signal is decomposed according to (B6) up to level 2 (formula 3) by using Daubechies wavelets of order 3, as is shown in Fig. 7. One can note that the maxima of the amplitude variation of d_1 and d_2 (defined in B2) coefficients correspond to the discontinuities of the first derivative of the signal, better represented by maxima of the d_1 coefficient amplitude (see Fig. 7).

Considering the amplitude of the detailed coefficients d_1 of the signal decomposition as a measure of the second derivative breakdown of the signal, we have calculated the averaged value of such coefficients for each year of the signal duration:

$$d_1(\text{year}(k)) = \sqrt{\frac{\sum_{i=1}^{12} (d_1(\text{year}(k), \text{month}(i)))^2}{12}} \quad (4)$$

SED
4, 131–172, 2012

Real data

Considering again the NGK observatory, a suitable de-noising of the monthly means of secular variation, without distortions of the signal itself, is achieved by using Daubechies wavelets of order 2/level 3–4, order 3/level 4, order 4/level 5–6 decompositions (see Fig. 8). From the previous tests we can conclude that the better way to detect particular events (defined as discontinuities of the first derivative of the field) in such a de-noised series is to use the Daubechies wavelets for the wavelet decompositions of level 2 of the same order as those used for the de-noising. Plotting the averaged values of detail coefficients d_1 (Fig. 8) of such decompositions, the geomagnetic jerks around 1969 and 1991 are clearly detected, while in a higher order decomposition events are noted around 1922 and 1941. This last event, not known as a regional or large-scale geomagnetic jerk, is related to changes of the secular variation slope due to several spikes close to each other.

We have then applied the same method to the monthly series of four geomagnetic observatories mentioned in Sect. 3.2.2. The results, not presented here, indicate that in order to get a reasonable de-noised signal, we have to use different order and level of wavelets for de-noising the monthly means, depending on the observatory. Different kinds of decompositions of the de-noised secular variation of Y component provided by the analyzed observatories underline different particular events, some of them corresponding to well-known geomagnetic jerks. However, we can note that from some observatory data, the presence of a large number of fringe (short spikes) in the de-noised signal make it difficult to detect geomagnetic jerks. This particularity is linked not only to the difference in length of geomagnetic recordings and the data quality provided by different observatories, but also to the different behavior of Y secular variation over the globe.

SED
4, 131–172, 2012

3.2.4 DWT applied to global model-based monthly means

Accepting that the amplitude variation of the detail coefficient (d_1) of the decomposition of the de-noised secular variation is an indicator of breakdowns in time-series of the second derivative of the geomagnetic field, we have composed the field of averaged amplitude of such a coefficient on the Earth's surface. As we need long time-series of uniformly distributed secular variation monthly estimates, the Gufm1 model can be used for this study. However, an important question can arise, linked to the possible signature of the B-splines nodes of the model in the wavelet analysis of synthetic series calculated from Gufm1 model. This has been investigated (but not shown here), and the effects of jerks are much larger, with different amplitudes and occurrence times, so the B-splines nodes are not relevant for our analyses.

We firstly investigate a single location series. Monthly values of SV_Y have been estimated at NGK coordinates, over a century (1890–1990), and the wavelet decomposition by the Daubechies wavelets of order 2/level 2 applied, which averaged detailed d_1 coefficients (Fig. 9). In order to detect particular events, we should consider only the values of d_1 coefficients larger than their average (0.004). Here, one can identify several events, that are undeniably known as large-scale extension (1969, 1978), or may have a similar extension (1913, 1925), or seems to be more local events (1906, 1919, 1949, 1958) (Alexandrescu et al., 1996; Le Huy et al., 1998; Mandea et al., 2010). The largest event is a local one that lasts from 1942 to 1949 and has a central maximum at 1946.

Thereafter, we have applied the wavelet analyses to the monthly values of SV_Y estimated from Gufm1 on a grid of 212 points uniformly distributed over the Earth's surface, for the period 1900–1990 Each series is decomposed by Db2 wavelets at level 2, saving the coefficients of decomposition. Then, we calculate the squared average value of such coefficients for every year of the considered period and plotted the field of d_1 coefficients for each epoch over the Earth. In Fig. 10, the fields of averaged d_1 coefficient for a selection of epochs are presented. As we plot the deviation of the d_1

SED
4, 131–172, 2012

coefficient value from its mean value of the whole period, the white areas correspond to regions where the d_1 values are smaller than the mean value and the black areas correspond to regions where values of the d_1 coefficient are greater than the maximum of the chosen scale. The plots of whole period can be seen in an additional animation (see supplemental material).

Let us discuss the behavior of the d_1 coefficient, as observed from plots and animation. It is indeed possible to note a relatively strong field in 1901, localized in four latitude belts mainly in the low and middle latitudes, which is followed by quiet fields from 1902 to 1904. Then two small spots of a strong field appear in 1905 over the Northern hemisphere, gradually enlarged and expanded even in the Southern hemisphere in 1910, 1911, 1912, to be reduced again in 1913.

Two other foci of strong field start in 1917, reaching a maximum next year and being reduced to a small spot in 1920. A quiet period follows until 1925, when a strong widespread field appears, and gradually reduces over the following years, with three remaining belts getting the strongest field on 1930–1932. From 1934 to 1940 a quiet period follows, with a few small spots at different locations, however insignificant.

From 1945 a strong field wide spreads until 1949, then two large belts of longitudes characterize the period 1950–1954. Similar shifted belts appear again in 1960, after a period of almost quiet field from 1954–1959, reaching their maxima in 1964. Another period of quiet field reaching the smallest value almost everywhere in 1967, is followed by a strong field reaching the maximum for the European area in 1969 and for a region situated in the Southern hemisphere in 1970.

Over the time period 1972–1978 a quiet field dominates with a few small spots of strong field near the South Pole. A strong field in 1978 is observed mainly in the large Western and Eastern longitude belts. A quiet field period ends in 1982 with the appearance of two local spots of strong field: one located around African continent and the other located in the large Western and Eastern longitudes. The latest one is faded gradually in the following years, while the first one reached maximum in 1985, moving thereafter toward the South Pole and splitting in two belts of strong field in 1987. The

SED
4, 131–172, 2012

strongest field in 1990 must be considered with caution because of the cutting edge effects.

3.3 Spherical Harmonic Power Spectra (SHPS)

The spherical harmonic analysis is a representation of the geomagnetic field potential as solution of Laplace equation. In order to detect any relation between the known jerk events and the time changes of the spherical harmonic of different degrees, we investigate the time variations of the Mauersberger-Lowes power spectrum terms of different degrees (Lowes, 1974, 2007) extending its definition to the third derivative of Gauss coefficients:

$$R_n^{3d} = \left(\frac{a}{r}\right)^{2n+4} (n+1) \sum_{m=0}^{n} \left[\left(\begin{matrix} \dots m \\ g_n \end{matrix} \right)^2 + \left(\begin{matrix} \dots m \\ h_n \end{matrix} \right)^2 \right] \quad (5)$$

with a = 6371.2 km = mean radius of the Earth. We estimate the spatial power spectrum of the third derivative since a geomagnetic jerk is defined as a step-like function in the second derivative of the geomagnetic field, thus it can be somehow related to extremes in the power spectral density of the third derivative, R_n^{3d}. We have used the CM4 model to calculate the time-series of the third derivative of the Gauss coefficients, using time increment: Δt = 2.5 years, over the time-span 1960–2002.5. When using smaller increment time some oscillations of values appear due to the spline approximation of values between knots of CM4 model. In Fig. 11, we present plots of R_n^{3d} evolution for different degrees (from $n = 1$ to $n = 12$) on the Earth's surface.

The behavior of R_n^{3d} at the CMB is similar, with the same relative minima and maxima, being just the same quantity scaled by a different radial ratio $(a/r)^{2n+4}$.

Supposing that occurrence date of the known jerks (1969, 1978, 1986, 1991, 1999) is in the middle of the year, the time interval (in years) of each jerk from the nearest maximum of R_n^{3td} is calculated for each degree n. These time intervals $\Delta t_{1969}(n)$, $\Delta t_{1978}(n)$, $\Delta t_{1986}(n)$, $\Delta t_{1991}(n)$, $\Delta t_{1999}(n)$ ($n = 1,2,\dots 12$) are presented in the second

SED
4, 131–172, 2012

row of Table 2, where the sign is (–) when the jerk happened before the nearest maximum and (+) when the jerk happened after the nearest maximum. In order to weight relatively the maxima of R_n^{3d} terms, we compute the quantity:

$$\gamma = ({R_n}^{3d}{}_{max} - {R_n}^{3d}{}_{min})/({R_n}^{3d}{}_{max} + {R^{3d}}_{min}) \quad (6)$$

where max and min indicate that values are at the nearest maximum or minimum. The weights γ range is $\{0,1\}$, and they are indicated in the first row characterizing each event. Weight of a maximum is an indicator about how clear and strong a jerk that occurs near that maximum is, which may be translated in a scale information.

Averaging the time between a given jerk date and the nearest maximum for all degrees ($n = 1,2,\ldots 12$) an averaged time-interval is obtained, listed in the penultimate column of the table:

$$\overline{\Delta t}_{1969} = \frac{\sum_i \Delta t^i_{1969}}{12}; \overline{\Delta t}_{1978} = \frac{\sum_i \Delta t^i_{1978}}{12}; \overline{\Delta t}_{1986} = \frac{\sum_i \Delta t^i_{1986}}{12}; \overline{\Delta t}_{1991} = \frac{\sum_i \Delta t^i_{1991}}{12}; \overline{\Delta t}_{1999} = \frac{\sum_i \Delta t^i_{1999}}{12} \quad (7)$$

In the last column of the table there are presented another kind of averaging, named in the table "averaged scaled time-interval". It is the average of the time-intervals from nearest maximum when these intervals are divided by the weight of respective maximum:

$$\overline{\Delta t}^s_{1969} = \frac{1}{12}\sum_i \frac{\Delta t^i_{1969}}{\gamma_{1969}}; \overline{\Delta t}^s_{1978} = \frac{1}{12}\sum_i \frac{\Delta t^i_{1978}}{\gamma_{1978}}; \ldots; \overline{\Delta t}^s_{1999} = \frac{1}{12}\sum_i \frac{\Delta t^i_{1999}}{\gamma_{1999}} \quad (8)$$

As the weights are smaller than 1, the divided time-intervals are increased in comparison to the respective time-intervals, and this increasing is as greater as smaller the weight of maximum is. In the last row of the table, there are shown the sums of time-intervals of all jerks for given degree and the respective sums when time-intervals are divided by the weight of the respective maximum (scaled time-intervals).

Analyzing the values indicated on columns (degrees) of Table 2 it appears that the best coincidences of the geomagnetic jerk dates with R_n^{3d} maxima are found for the

SED
4, 131–172, 2012

degrees $n = 5$ and $n = 9$. When we consider the sum of scaled time-intervals there is little deterioration for $n = 5$ in comparison to $n = 9$. According to this, we can estimate a spreading of the geomagnetic jerks by comparing it to the wavelengths of these harmonics ($n = 5$ and $n = 9$) given by $\frac{2\pi}{n+1/2} \cdot r$ (Backus et al, 1996). The obtained spatial scales of about 7300 and respectively 4230 km are a confirmation of estimates from the d_1 coefficient field analysis, previously shown, where regions of the strong fields possess these spatial scales.

Analyzing Table 2 rows, in terms of geomagnetic jerks, it appears that events around 1969, 1978 and 1999 occur at the shorter averaged time-intervals from the maximums of R_n^{3d} (if we except $n = 1$, then these time-intervals vary from 1.5 to 2 years), while the events around 1986 and 1991 occur at longer time-intervals from maximums of R_n^{3d} (4–6.5 years). The same results are indicated by the row of averaged scaled time-intervals We can consider the jerks of 1986 and 1991 more than others as local events.

As errors for each Gauss coefficients and their derivatives of CM4 model are not available, it is difficult to analyze the robustness of time-series of R_n^{3d} . We know that errors of coefficient derivative errors are at least one order smaller than the respective values of coefficient derivatives. Then, errors of R_n^{3d} are at least one order lower than the respective values of R_n^{3d}. Regarding the deviations of the real values of the third derivative of field values and the respective third derivative of the model field values, we can suggest that their RMS should have oscillations for different degree (like secular variation, see Sabaka et al., 2004), that are not important for our analyses.

4 Discussions and conclusions

Understanding the origin of rapid changes of the geomagnetic field arising from inside the Earth is challenging. The recent joint analysis of ground-based and satellite data has brought some progress, mainly because of their very different distributions in space and in time. Nevertheless, such new data are available only over the last decade, and there is a clear need to apply new mathematical techniques to geomagnetic series covering longer periods.

SED
4, 131–172, 2012

Here, we show that a specific behavior of geomagnetic jerks can be noted mostly in different longitude belts. Particular events, having as signatures strong fields of the d_1 coefficients, are not extended over the whole globe. As shown by the available animation, starting with the 1901 event, the strong field is concentrated mostly in four longitudinal belts. The known extended 1913 jerk is represented by a strong field during 1910–1911, while the one in 1925 is represented by a strong field in four large longitudinal belts (the largest one in the center). An event around 1932 is presented by the strong field in the longitudinal belts from 1930–1932. The event of 1949 is characterized by a strong field that lasts for the longest period of time (1945–1951), covering almost half of the globe. The well known geomagnetic jerk in 1969 is presented by a spot over Europe and an Eastern belt of strong fields during 1968–1969, followed by two large belts of strong field during 1970–1971 and the relatively strong field in the Southern hemisphere in 1972. The 1978 geomagnetic jerk is shown by local foci of strong field over some regions of the Earth. Finally, the event in 1986 is represented by a strong field mostly over the Southern African and the south Pole region. Apart from these events corresponding to geomagnetic jerks already noted in literature, the d_1 coefficients indicate additional particular events, especially in 1917–1918, 1945–1946, 1952–1954, 1963–1965, until now not reported as possible geomagnetic jerks.

Recently, Olsen and Mandea (2008) have shown that changes in the core magnetic field can be as short as a few months. These rapid secular variation fluctuations are not globally observed from satellite data. Our results based on both observatory and synthetic data are a complement of previous studies investigating the geomagnetic jerks or rapid secular variation fluctuations spatial distribution, and illustrate, with results covering nearly one century, that these events are not global in appearance. Also the unbalanced contributions of the spherical harmonic degrees at the different jerks are intriguing and deserve deeper attention in further studies and analyses. To conclude, all these findings are important for continuing the present investigations on jerks to uncover more details and features of the core dynamics.

SED
4, 131–172, 2012

Appendix A

The DFT definition

The most general form of Fourier transform $X(\omega)$ or $X(f)$ of a continuous time function $x(t)$, and its inverse transform are:

$$X(\omega) = \int_{-\infty}^{\infty} x(t)e^{-j\omega t}dt \quad \text{or} \quad X(f) = \int_{-\infty}^{\infty} x(t)e^{-j2\pi ft}dt \tag{A1}$$

$$x(t) = \frac{1}{2\pi}\int_{-\infty}^{\infty} X(\omega)e^{j\omega t}d\omega \quad \text{or} \quad x(t) = \int_{-\infty}^{\infty} X(t)e^{-j2\pi ft}df \tag{A2}$$

where $f = \omega / 2\pi$ is the frequency.

A discrete time function can be considered as a sequence of samples of a continuous time function. The time interval between two consecutive samples $x[m]$ and $x[m+1]$ is $t_0 = 1/f_s$, where f_s is the sampling rate, which is also the period of the spectrum in the frequency domain. The Fourier transform and the inverse transform of this function are (Brockwell and Davis, 2009):

$$X_F(f) = \sum_{m=-\infty}^{\infty} x[m]e^{-j2\pi fmt_0}, \quad \text{and} \quad x[m] = \frac{1}{f_s}\int_{-f_s/2}^{+f_s/2} X_F e^{-j2\pi fmt_0}df \tag{A3}$$

$(m = 0, \pm 1, \pm 2, \ldots)$.

When the discrete time function is given in a limited time interval T, its periodic discrete time function $x[m]$ with period T has periodic spectrum $X[n]$, given by discrete Fourier transform (DFT) and its inverse:

$$X[n] = \frac{1}{T}\sum_{m=0}^{N-1} x[m]e^{-j2\pi nmf_0t_0}, \quad \text{and} \quad x[m] = \frac{1}{f_s}\sum_{n=0}^{N-1} X[n]e^{j2\pi nmf_0t_0} \tag{A4}$$

SED
4, 131–172, 2012

where m, $n = 0,1,2,\ldots, N-1$; N is the number samples in the period T, which is also the number of frequency components in the spectrum:

$$N = \frac{T}{t_0} = \frac{1/f_0}{1/f_s} = \frac{f_s}{f_0} \tag{A5}$$

The DFT can be redefined as in FFT algorithm:

$$X[n] = \frac{1}{\sqrt{N}} \sum_{m=0}^{N-1} x[m] e^{-j2\pi nm/N}, \text{ and } x[m] = \frac{1}{\sqrt{N}} \sum_{n=0}^{N-1} X[n] e^{j2\pi nm/N} \tag{A6}$$

If $x[m]$ is real, then we have: $X[n] = X^*[n]$

The STFT definition

The Short Time Fourier Transform (STFT) of one-dimensional continuous time is the Fourier Transform of the function $x(t)$ multiplied by a window function, where the window is slid along the time axis, resulting in a two-dimensional representation of the signal (Jacobsen and Lyons, 2003):

$$X(\tau,\omega) = \int_{-\infty}^{\infty} x(t) w(t-\tau) e^{-j\omega t} dt \tag{A7}$$

where $w(t)$ is the window function, commonly a Gaussian-form centered around zero. Generally, $X(\tau,\omega)$ is a complex function representing the phase and magnitude of the signal over time and frequency. The magnitude squared of the STFT yields the spectrogram of the function:

$$\text{spectrogram}\{x(t)\} \equiv |X(\tau,\omega)|^2 \tag{A8}$$

In the discrete time case, the data to be transformed are broken up into blocks, which usually overlap each other. Each block is Fourier transformed, and the complex result

SED
4, 131–172, 2012

is added to a matrix, which records magnitude and phase for each point in time and frequency. This can be expressed as:

$$\mathrm{STFT}\{x[m]\} \equiv X(k,\omega) = \sum_{m=-\infty}^{\infty} x[m]w[m-k]e^{-jmt_0\omega} \tag{A9}$$

likewise, with discrete signal $x[m]$ and discrete window $w[m]$, while the frequency $\omega = 2\pi f$ is continuous. But in most typical applications the STFT is performed on a computer using the Fast Fourier Transform algorithm, so both variables are discrete and quantized: $m = 0,1,2,\ldots N-1$ and $f = n \cdot f_0 = n \cdot f_s/N = n/(t_0 \cdot N)$ $(n = 0,1,2,\ldots, N-1)$. Then the STFT is defined as:

$$\mathrm{STFT}\{x[m]\} \equiv X(k,n) = \sum_{m=0}^{N-1} x[m]w[m-k]e^{-j2\pi mn/N} \tag{A10}$$

where $k = 0,1,2,\ldots, N-1$, and the spectrogram is defined as:

$$\mathrm{spectrogram}\{x[m]\} \equiv |X(k,n)|^2 \tag{A11}$$

The MatLlab function:

B = specgram (***x***, *nfft*, f_s, window (length), numoverlap)

calculates the windowed discrete-time Fourier transform for the signal in vector x with length N; *nfft* specifies the FFT length that specgram uses, f_s specifies the sampling frequency, window specifies a windowing function and the number of samples specgram uses in its sectioning of vector ***x***. If ***x*** is real, specgram computes the discrete-time Fourier transform at positive frequencies only. If N is even, specgram returns *nfft*/2+1 rows (including the zero and Nyquist frequency terms). If n is odd, specgram returns *nfft*/2 rows. The number of columns in B is the integer number (fix number) of (N-numoverlap)/(length(window)-numoverlap))

The spectrogram figure windows, present in time-frequencies axis the plots of the scaled logarithmic (in dB) amplitudes: 20*$\log_{10}$(abs(B)).

SED
4, 131–172, 2012

Appendix B

The continuous wavelet transform (CWT) of a time function $s(t)$ is defined as the integral over all time of the signal multiplied by scaled (dilated) and shifted (translated) versions of the wavelet function Ψ (Misiti et al., 2007):

$$T(a,b) = \int_{-\infty}^{\infty} s(t)\Psi(a,b,t)dt \tag{B1}$$

with a = scale, b = position. If a function Ψ is continuous, has null moments, decreases quickly towards 0 when t tends towards infinity, or is null outside a segment of R, it is a likely candidate to become a wavelet. Scaling (dilating) a wavelet simply means stretching (or compressing) it by a scale factor a. The smaller the scale factor, the more "compressed" the wavelet. Shifting (translating) a wavelet simply means delaying (or hastening) its onset. The wavelet decomposition consists of calculating a "resemblance coefficient" between the signal and the wavelet located at position$b$ and of scale a. The family of such coefficients $C(a,b)$ depends on two indices a and b (Kumar and Georgiu, 1994):

$$C(a,b) = \int_R s(t)\frac{1}{\sqrt{a}}\Psi\left(\frac{t-b}{a}\right)dt \tag{B2}$$

In the CWT, the set to which a and b belong is: $a \in R^+ - \{0\}$, $b \in R$.In the Discrete Wavelets Transform (DWT), the scale parameter a and the location parameter b are discrete, usually based on powers of two: $a = 2^j$, $b = k \cdot 2^j$, $(j, k) \in Z^2$ (so-called dyadic scales and positions).

We define:

$$\psi_{j,k}(t) = \frac{1}{\sqrt{2^j}}\psi\left(\frac{t-k2^j}{2^j}\right) = 2^{-j/2}\psi\left(2^{-j}t-k\right), \tag{B3}$$

SED
4, 131–172, 2012

identifying $\Psi_{00}(t) = \Psi(t)$.

It is possible to construct a certain class of wavelets $\Psi(t)$ such that $\Psi_{j,k}(t)$ are orthonormal, i.e. the wavelets are orthogonal to their dilates and translates:

$$\int \psi_{j,k}(t)\psi_{j',k'}(t)dt = \delta_{jj'}\delta_{kk'}.$$

This implies that all such functions $\Psi_{j,k}(t)$ form a complete orthonormal basis for all functions $s(t)$ that have finite norm, i.e.: the time signal $s(t)$ is expressed by the coefficients of discrete wavelet decomposition $C(j,k)$ as:

$$s(t) = \sum_{j\in Z}\sum_{k\in Z} C(j,k)\psi_{j,k}(t), \text{ where } C(j,k) = \langle s, \psi_{j,k}\rangle \equiv \int s(t)\psi_{j,k}(t)dt \tag{B4}$$

Let us fix j and sum on k. A detail d_j is then the function:

$$d_j(t) = \sum_{k\in Z} c(j,k)\psi_{j,k}(t) \tag{B5}$$

The signal is the sum of all the details:

$$s = \sum_{j\in Z} d_j \tag{B6}$$

Let us take now a reference level called J. There are two sorts of details. Those associated with indices $j \leq J$ correspond to the scales $a = 2^j \leq 2^J$ which are the fine details. The others, which correspond to $j > J$, are the coarser details. We group these latter details into:

$$a_J = \sum_{j>J} d_j \tag{B7}$$

which defines what is called an approximation of the signal s. We have just created the details and an approximation. The equality:

$$s = a_J + \sum_{j\leq J} d_j \tag{B8}$$

SED
4, 131–172, 2012

means that the signal s is the sum of its approximation a_J and of its fine details d_j.

Appendix C

WARMA – noise generation

"warma" is a colored AR(3) noise generated by MATLAB from the formula:

$$b_2(t) = -1.5b_2(t-1) - 0.75b_2(t-2) - 0.125b_2(t-3) + b_1(t) + 0.5,$$

$b_1(t)$ being a uniform white noise series.

The test of normal probability plot shows that the underlying distribution of the "warma" series for $t = 1,2,3\ldots$, 1000, is a normal one, with variance = 0.6135 and sigma = 0.78326.

The following changes on "warma" signal provide a more realistic noise (more like the noise of a secular variation signal). From a 125-value long colored noise (warma(1:125), variance = 0.6079, sigma = 0.7797)) we generated a more extended noise (1000 value long), where 8 values between each couple of successive values are generated by adding proportionally the difference between these successive values. The test of normal probability plot shows a slight deviation from the normal distribution, with variance = 0.2284 and sigma = 0.4779. Each value is multiplied by certain number such that the amplitude of the noise reaches about 15 % of the signal amplitude (the signal composed by differences of several exponential spikes like (1).

Acknowledgements. The authors wish to thank S. Mackmillan and A. Chambodut for their helpful comments and remarks regarding the first version of the manuscript.

Supplementary material related to this article is available online at: http://www.solid-earth-discuss.net/4/131/2012/sed-4-131-2012-supplement.zip.

SED
4, 131–172, 2012

References

Alexandrescu, M., Gilbert, D., Hulot, G., Le Mouël, J.-L., and Saracco, G.: Detection of geomagnetic jerks using wavelet analysis, J. Geophys. Res., 100, 12557–12572, 1995.

Alexandrescu, M., Gilbert, D., Hulot, G., Le Mouël, J.-L., and Saracco, G.: Worldwide wavelet analysis of geomagnetic jerks, J. Geophys. Res., 101, 21975–21994, 1996.

Backus, G., Parker, R., and Constable, C.: Foundation of Geomagnetism, Cambridge University Press, 103, 1996.

Benton, E. R., Estes, R. H., and Langel, R. A.: Geomagnetic field modeling inconrporating constraints from frozen flux electromagnetism, Phys. Earth Planet. Inter., 48, 241–264, 1987.

Bloxham, G., Zatman, S., and Dumberry, M.: The origin of geomagnetic jerks, Nature, 420, 65–68, 2002.

Brockwell, P. J. and Davis, R. A.: time-series: Theory and Methods, 2 Edn., Springer, 2009.

Chambodut, A. and Mandea, M.: Evidence for geomagnetic jerks in comprehensive models, Earth, Planet. Space, 57, 139–149, 2005.

Chambodut, A., Panet, I., Mandea, M., Diament, M., Holschneider, M., and James, O.: Wavelet frames: an alternative to spherical harmonic representation of potential fields, Geophys. J. Int., 163, 875–899, 2005.

Chau, H. D., Ducruix, J., and Le Mouël, J.-L.: Sur le caractère planétaire du saut de variation séculaire de 1969–1970, C. R. Acad. Sci. Paris, B293, 157–160, 1981.

Courtillot, V., Ducruix, J., and Le Mouël, J.-L.: Sur une accélérations récente de la variation séculaire du champ magnétique terrestre, C. R. Acad. Sci. Paris, D287, 1095–1098, 1978.

Daubechies, I.: Ten lectures on wavelets, CBMS-NSF Regional Conference Series in Applied Mathematics, Society for Industrial and Applied Mathematics, Philadelphia, 1992.

Gabor, D.: Theory of communications, J. Inst. Elec. Eng., 93, 429–457, 1946.

Grossmann, A., Holschneider, M., Kronland-Martinet, R., and Morlet, J.: Detection of abrupt changes in sound signals with the help of wavelet transform, in: Inverse Problems: An Interdisciplinary Study, Adv. Electron. Electron. Phys., 19, San Diego, CA: Academic, 298–306, 1987.

Holschneider, M.: Wavelets: An Analysis Tool, Oxford: Oxford University Press, 1995.

Jacobsen, E. and Lyons, R.: The sliding DFT, Signal Processing Magazine, 20, 74–80, 2003.

Jackson, A., Jonkers, A. R. T., and Walker, M. R.: Four centuries of geomagnetic secular variation from historical records, Phil. Trans. R. Soc. Lond., 358, 957-990, 2000.

SED
4, 131–172, 2012

Kumar, P. and Georgiu, E. F.: Wavelet Analysis in Geophysics: An Introduction, in Wavelet Analysis and its Applications, 1–43, Academic Press, 1994.
Le Huy, M., Alexandrescu, M., Hulot, G., and Le Mouël, J.-L.: On the characteristics of successive geomagnetic jerks. Earth Planets Space, 50, 723–732, 1998.
Lowes, F. J.: Spatial power spectrum of the main geomagnetic field, and extrapolation to the core, Geophys. J. R. Astr. Soc., 36, 717–730, 1974.
Lowes, F. J.: Spatial Geomagnetic Spectrum, in Encyclopedia of geomagnetism and paleomagnetism, edited by: Gubbins, D. and Herrero-Bervera, E., Springer, 351–353, 2007.
MATLAB: the language of technical computing. Using MATLAB, MathWorks Inc., 2004.
Mandea, M., Bellanger, E., and Le Mouël, J. -L.: A geomagnetic jerk for the end of the 20th century?, Earth Planet. Sci. Lett., 183, 369–373, 2000.
Mandea, M., Holme, R., Pais, A., Pinheiro, K., Jackson, A., and Verbanac, G.: Geomagnetic Jerks: Rapid Core Field Variations and Core Dynamics, Space Sci. Rev., 155, 147–175, 2010.
Meyer, Y.: Wavelets and Operators, Cambridge University Press, 1992.
Meyer, Y.: Wavelets, Algorithms and Applications, SIAM, Philadelphia, 1993.
Misiti, M., Misiti, Y., Oppenheim, G., and Poggi, J. M.: Wavelets and Their Applications, Hermes Lavoisier, ISTE Publishing Knowledge, 2007.
Nagao, H., Iyemori, T., Higuchi, T., and Araki, T.: Lower mantle conductivity anomalies estimated from geomagnetic jerks, J. Geophys. Res., 108, 2254, doi:10.129/2002JB001786, 2003.
Olsen, N. and Mandea, M.: Investigation of a secular variation impulse using satellite data: The 2003 geomagnetic jerk, Earth Planet. Sci. Lett., 255, 94–105, 2007.
Olsen, N. and Mandea, M.: Rapidly changing flows in the Earth's core, Nat. Geosci., 1, 390–394, 2008.
Oppenheim, A. V. and Schafer, R. W.: Discrete-Time Signal Processing, Prentice Hall, Englewood Cliffs, NJ, 1989.
Sabaka, T. J., Olsen, N., and Langel, R. A.: A comprehensive model of the quiet-time, near-Earth magnetic field: Phase 3, Geophys. J. Int., 151, 32–68, 2002.
Sabaka, T. J., Olsen, N., and Purucker, M. E.: Extending comprehensive models of the Earth's magnetic field with Ørsted and CHAMP data, Geophys. J. Int., 159, 521–547, 2004.
Stewart, D. N. and Whaler, K. A.: Geomagnetic disturbance fields: an analysis of observatory monthly means, Geophys. J. Int., 108, 215–223, 1992.

SED
4, 131–172, 2012

Table 1. The geomagnetic observatories that have been chosen as representatives for analyses.

IAGA code	Latitude	Longitude	Altitude (m)
API	–13°48′	188°13.2′	4
HER	–34°25.2′	19°13.8′	26
KAK	36°13.8′	140°11.4′	36
NGK	52°4.2′	12°40.8′	78

SED
4, 131–172, 2012

Table 2. Geomagnetic jerk dates correspondences to the R_n^{3d} maxima.

	$n=1$	$n=2$	$n=3$	$n=4$	$n=5$	$n=6$	$n=7$	$n=8$	$n=9$	$n=10$	$n=11$	$n=12$	Averaged time-intervals (year)	Averaged scaled time-intervals
1969.5	0.850 −13	0.207 −0.5	0.019 −0.5	0.332 4.5	0.831 −0.5	0.697 −0.5	0.958 2	0.811 2	0.944 2	0.634 2	0.479 2	0.150 2	2.791	7.186
1978.5	0.850 −4	0.221 −4	0.344 −4	0.391 1	0.574 −1.5	0.713 −1.5	0.181 1	0.173 1	0.726 1	0.178 −1.5	0.402 1	0.650 1	1.876	5.57
1986.5	0.802 4	0.199 4	0.815 4	0.541 1.5	0.286 −3.5	0.766 6.5	0.725 4	0.112 4	0.636 4	0.692 6.5	0.350 4	0.272 −8.5	4.541	12.757
1991.5	0.907 −6	0.761 −6	0.913 −6	0.330 −3.5	0.215 1.5	0.766 +11.5	0.725 9	0.835 −8.5	0.395 −1	0.690 −11	0.248 −8.5	0.272 −3.5	6.333	11.823
1999.5	0.907 +2	0.526 2	0.913 2	0.023 −0.5	0.761 −0.5	0.895 −3	0.865 −3	0.835 −0.5	0.851 −0.5	0.690 −3	0.361 −0.5	0.166 −0.5	1.5	3.945
Sum	33.81 29	52.30 16.5	51.61 16.5	51.23 11	23.09 7.5	29.67 23	29.01 19	54.74 16	12.90 8.5	41.26 24	53.75 16	62.00 15.5	← Sum of Scaled time-intervals ← Sum of Nonscaled time-intervals	

SED
4, 131–172, 2012

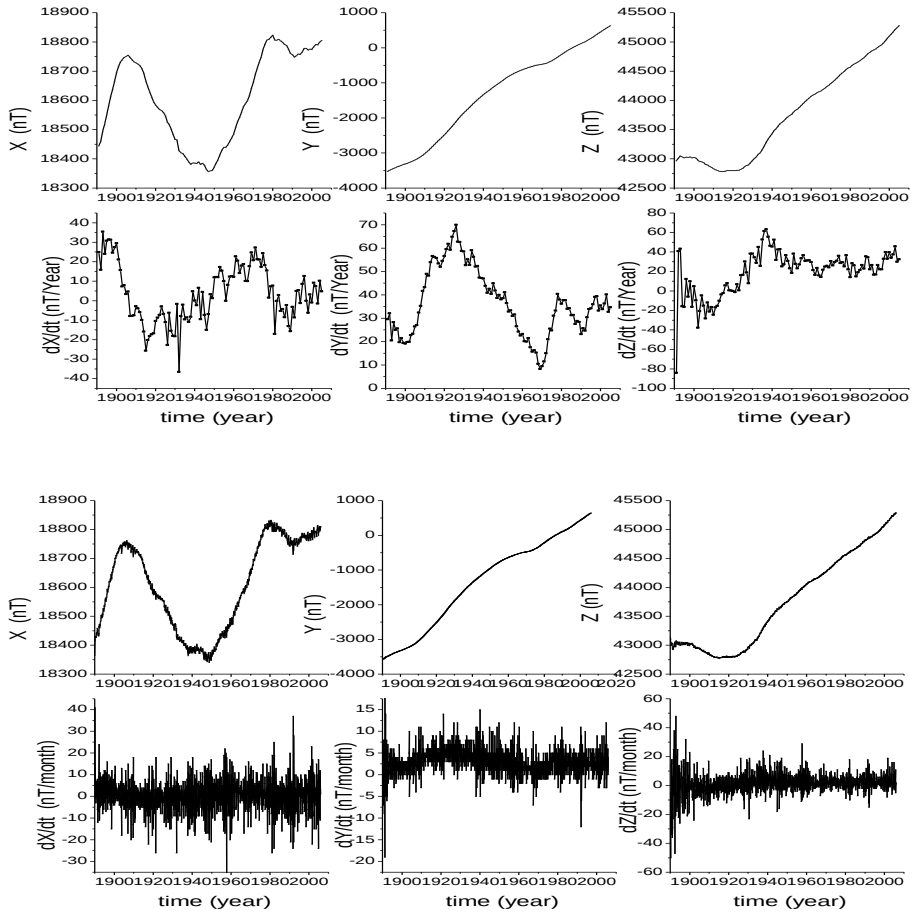

Fig. 1. Annual (upper) and monthly (lower) mean series of X, Y, Z components and their numerical derivatives (differences of the sequential values).

SED
4, 131–172, 2012

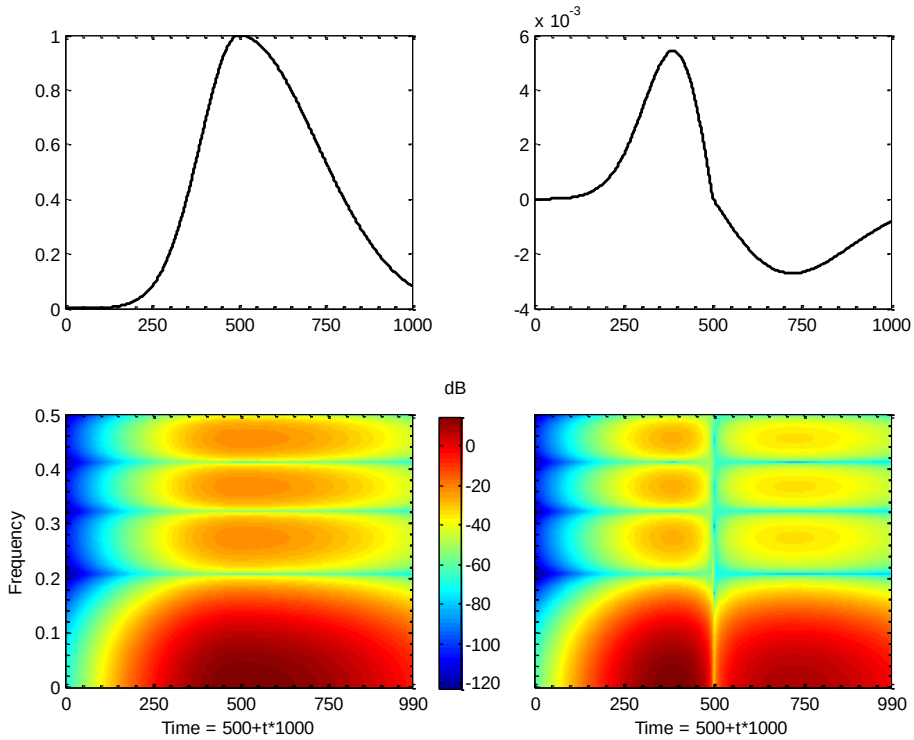

Fig. 2. The signal (1) (up left) sampled at every $\Delta t = 10^{-3}$ with the temporal abscissa rescaled as time = 500 + t·1000, and the spectrogram of the signal (down left) and the first difference series (upper right) and its spectrogram (down right). The units are arbitrary.

SED
4, 131–172, 2012

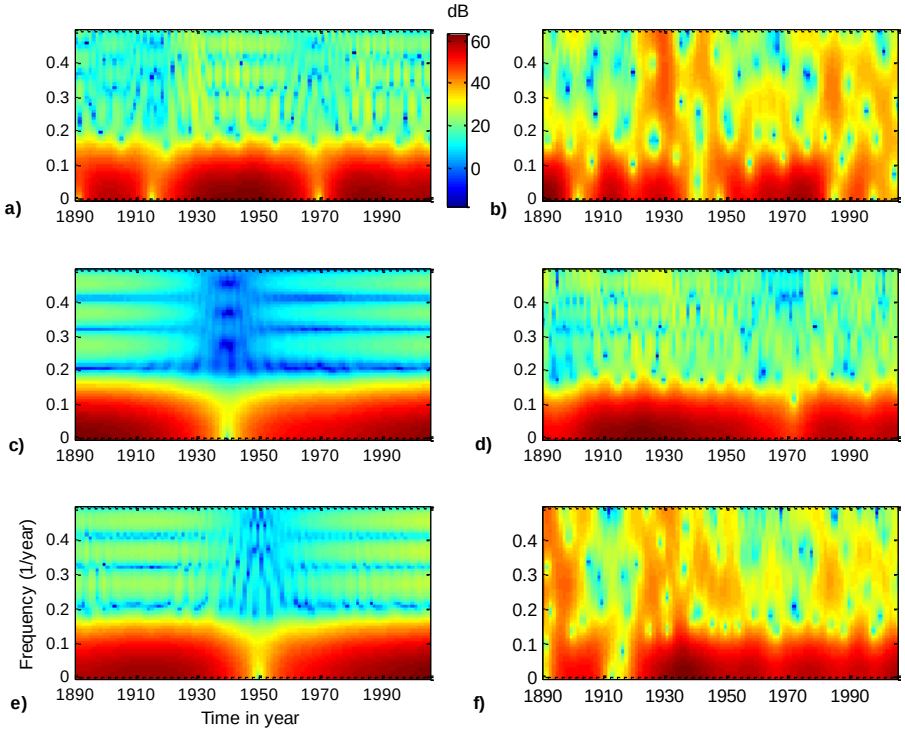

Fig. 3. Spectrograms of annual means of the geomagnetic field components and their secular variation (first differences) for NGK observatory (1890–2005): **(a)** X component, **(b)** X secular variation, **(c)** Y component, **(d)** Y secular variation, **(e)** Z component, **(f)** Z secular variation.

SED
4, 131–172, 2012

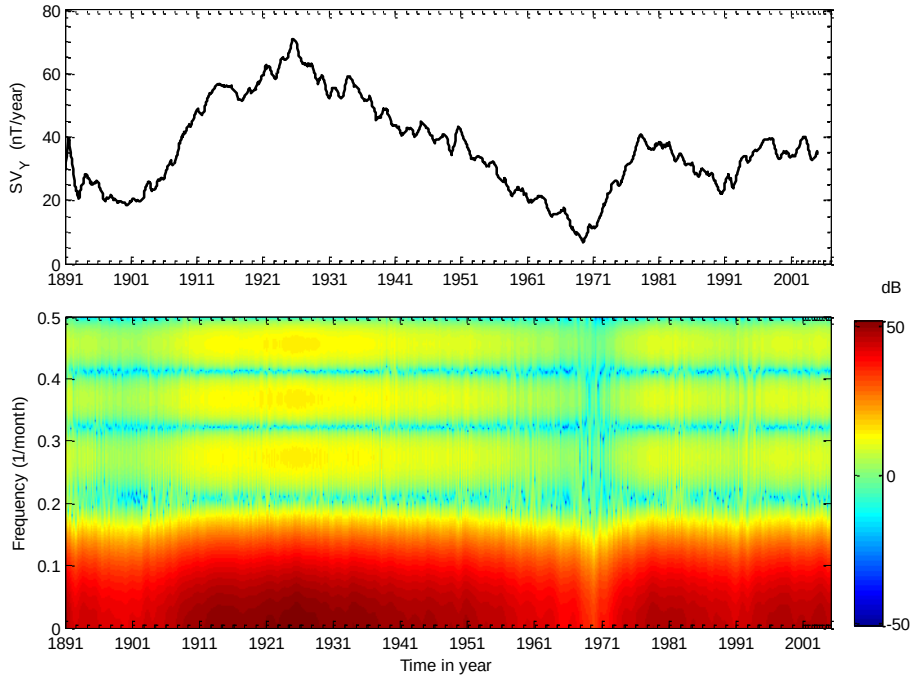

Fig. 4. The monthly means of SV_Y (upper panel) calculated by 12-month averaging window from monthly values of Y-component provided by NGK observatory (1890–2005) and its spectrogram (bottom panel).

SED
4, 131–172, 2012

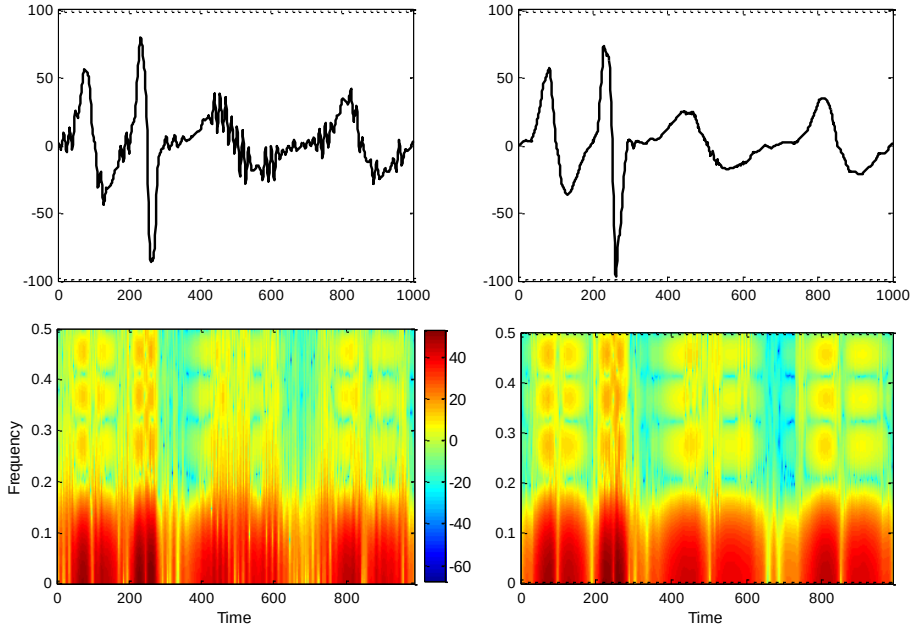

Fig. 5. Synthetic signal representing a secular variation-like signal (top panel, left) composed by first differences of several exponential spikes plus a colored noise and the corresponding spectrogram (bottom panel, left). The de-noised signal (top panel, right) and its corresponding spectrogram (bottom panel, right). The units are arbitrary.

SED
4, 131–172, 2012

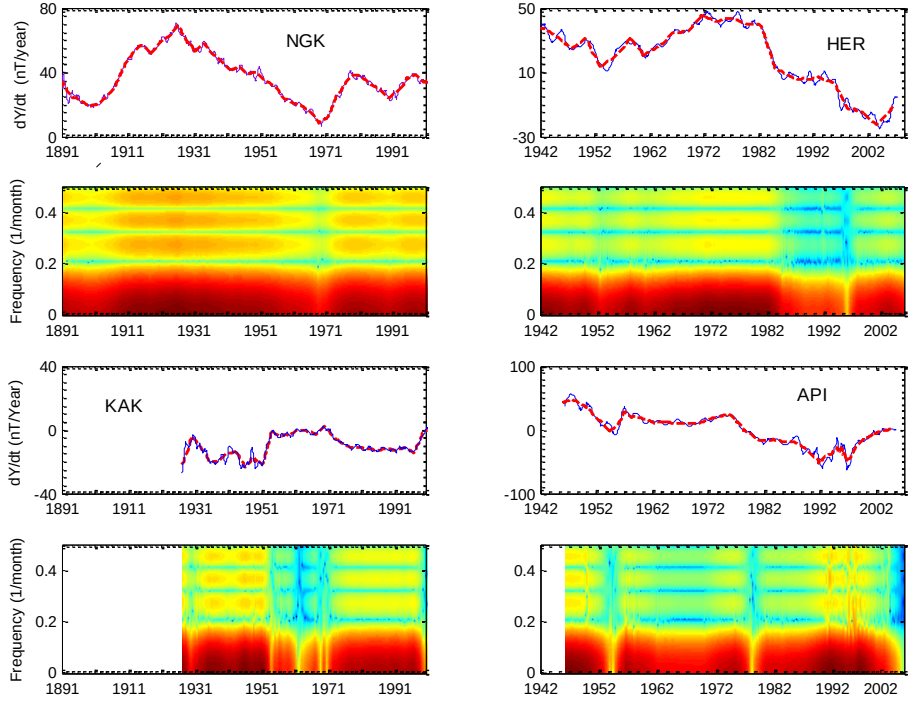

Fig. 6. The signals (blue curves) and de-noised signals (red curves) of secular variations (SV_y = dY/dt) of NGK, KAK, API and HER observatories and their respective spectrograms derived from application of STFT on these signals.

SED
4, 131–172, 2012

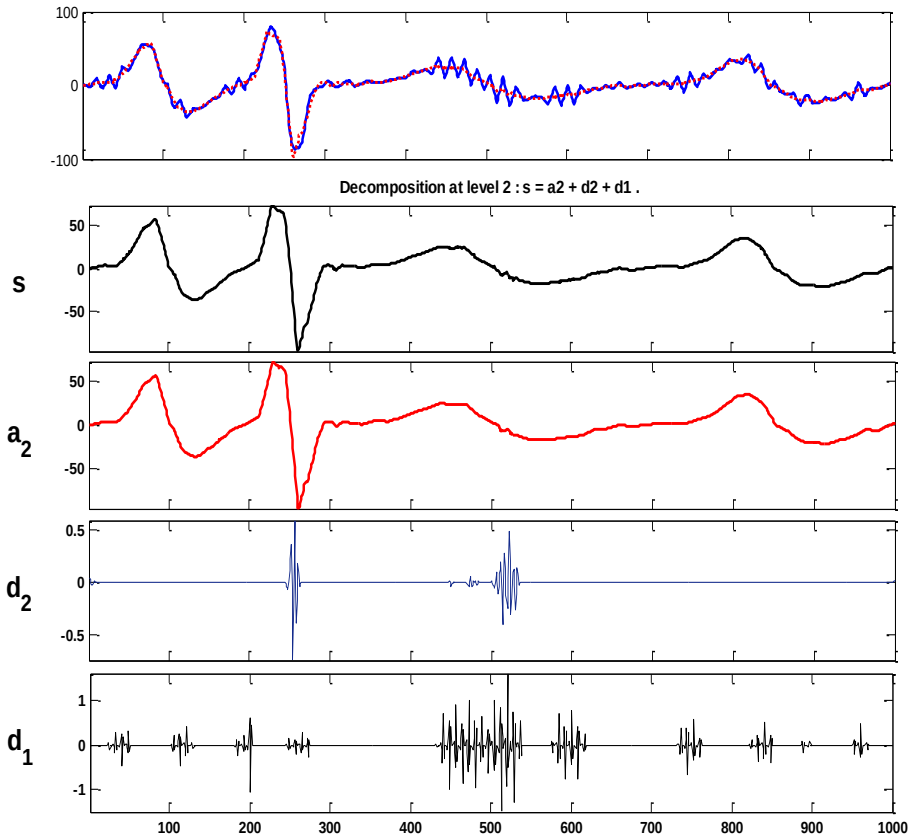

Fig. 7. The synthetic composed signal (different exponential spikes + colored noise) and its de-noised signal (up); the decomposition of the de-noised signal up to level 2 (down). Units are arbitrary, although they would resemble time in years and SV in nT/yr, in the x and y axes, respectively. The units are arbitrary.

SED
4, 131–172, 2012

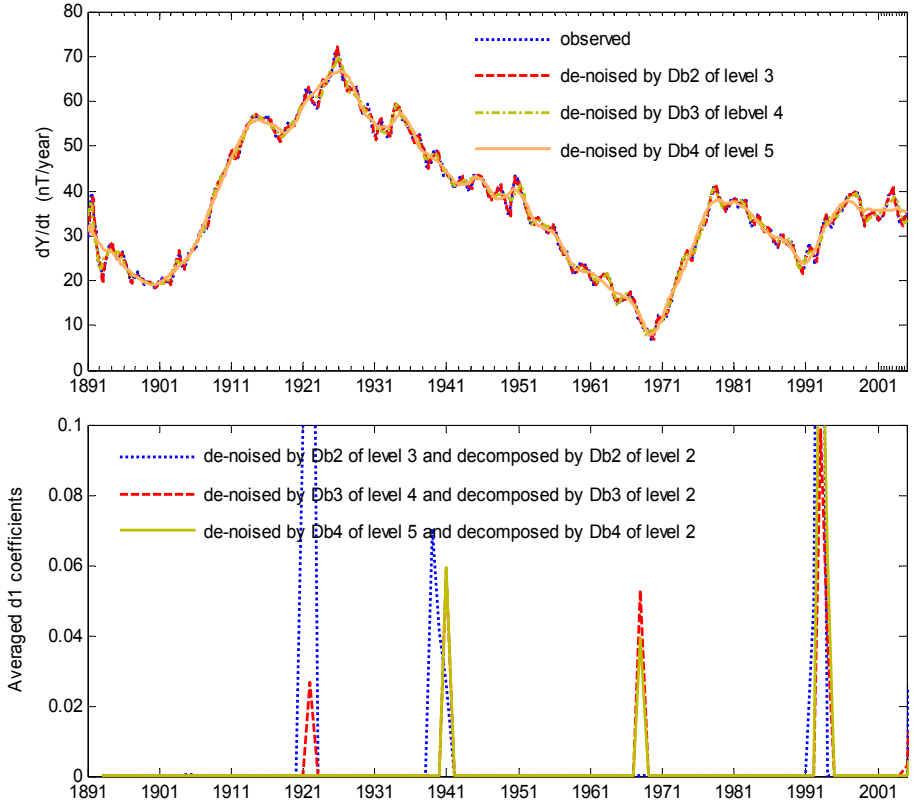

Fig. 8. De-noised SV_Y signal of NGK (up) and the respective values of averaged d_1 coefficients (down). The unit of d_1 coefficients are in nT/year.

SED
4, 131–172, 2012

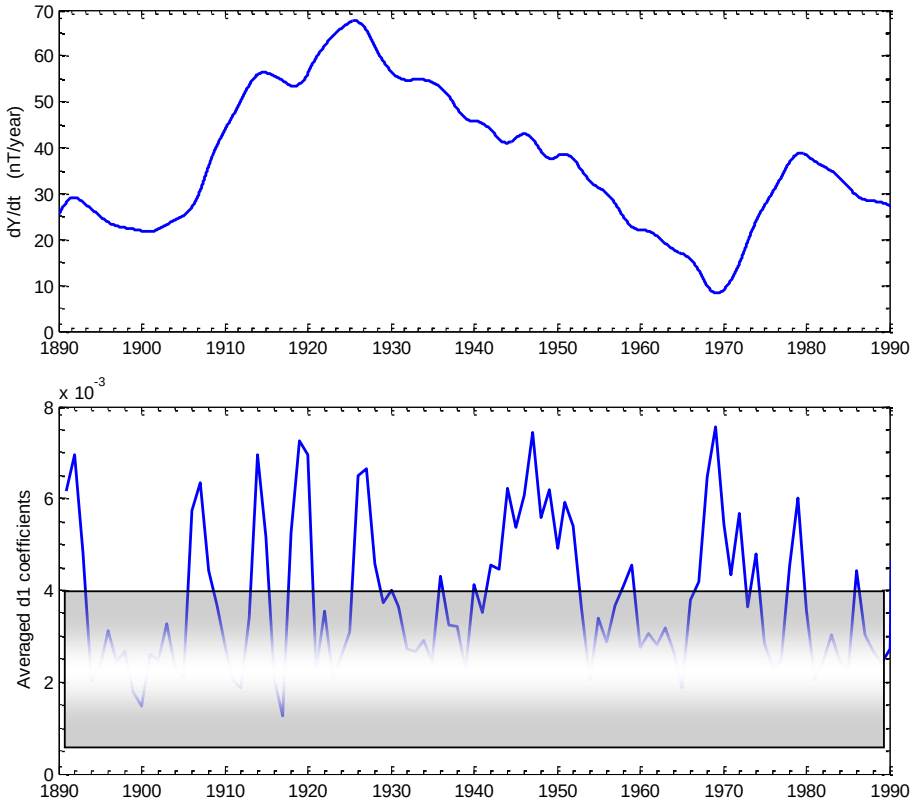

Fig. 9. Monthly series of secular variation of Y component generated by Gufm1 model at NGK Observatory for the period 1890–1990 (upper panel) and averaged d_1 coefficients of the series decomposition by Db2 wavelets of level 2. The d_1 coefficients (in nT/year) below their mean value are covered.

SED
4, 131–172, 2012

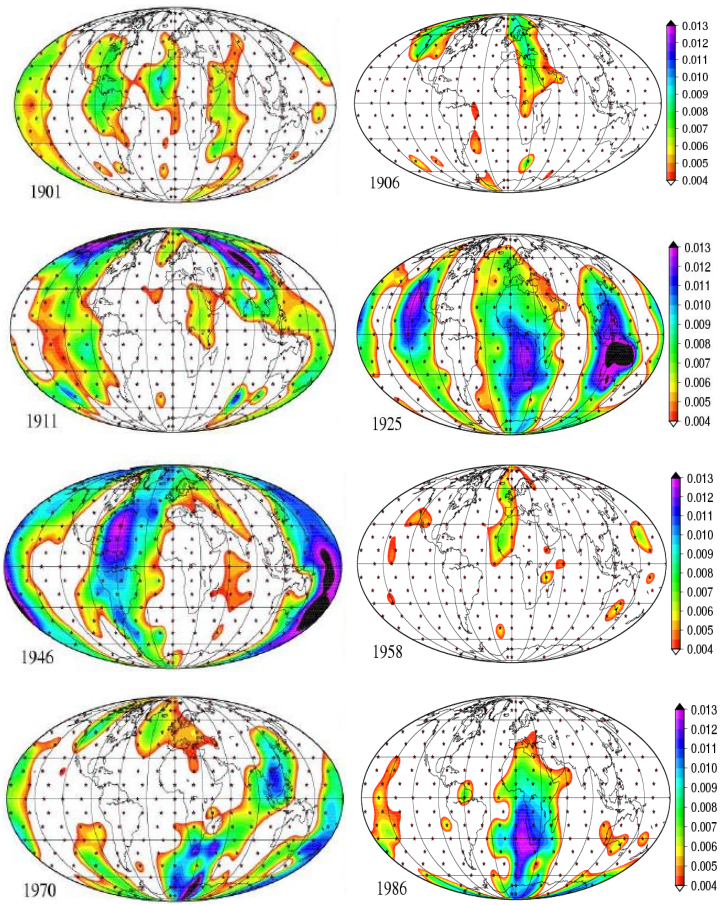

Fig. 10. An example of the d_1 coefficient field behavior, for the epochs: 1901, 1906, 1911, 1925, 1946, 1958, 1970, 1986, which are a selection from the complete animation in the supplemental material. Units are in nT/yr.

SED
4, 131–172, 2012

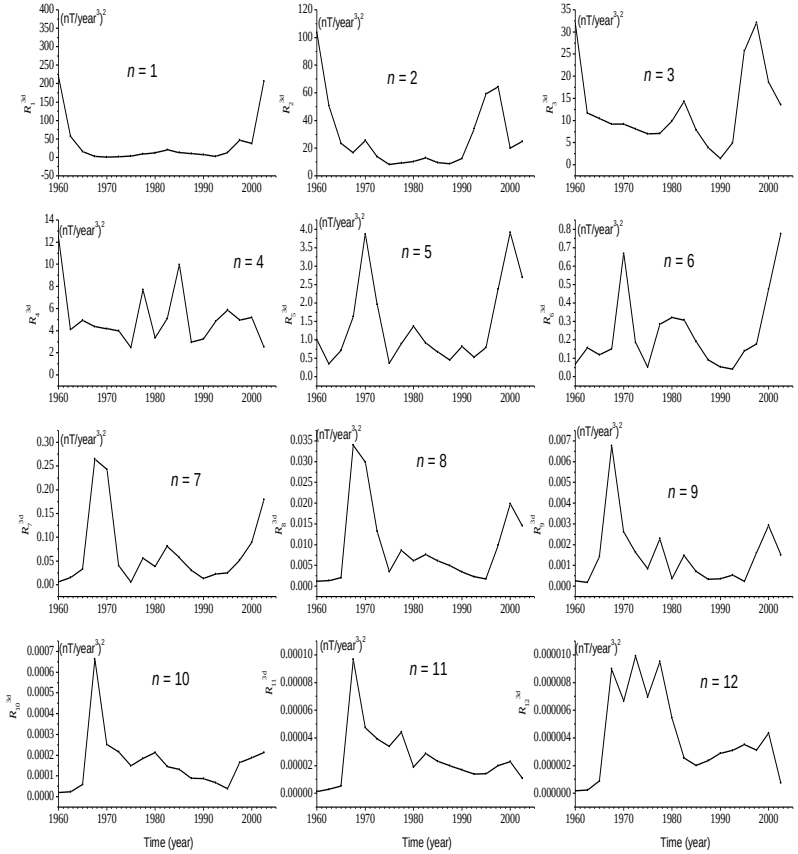

Fig. 11. Time variations of the spherical harmonic power spectra terms (R_n^{3d}) at the Earth's surface.

SED
4, 131–172, 2012